Volume 7 | Number 23 | 21 June 2019 | Pages 13793–14338

Journal of Materials Chemistry A

Materials for energy and sustainability

rsc.li/materials-a

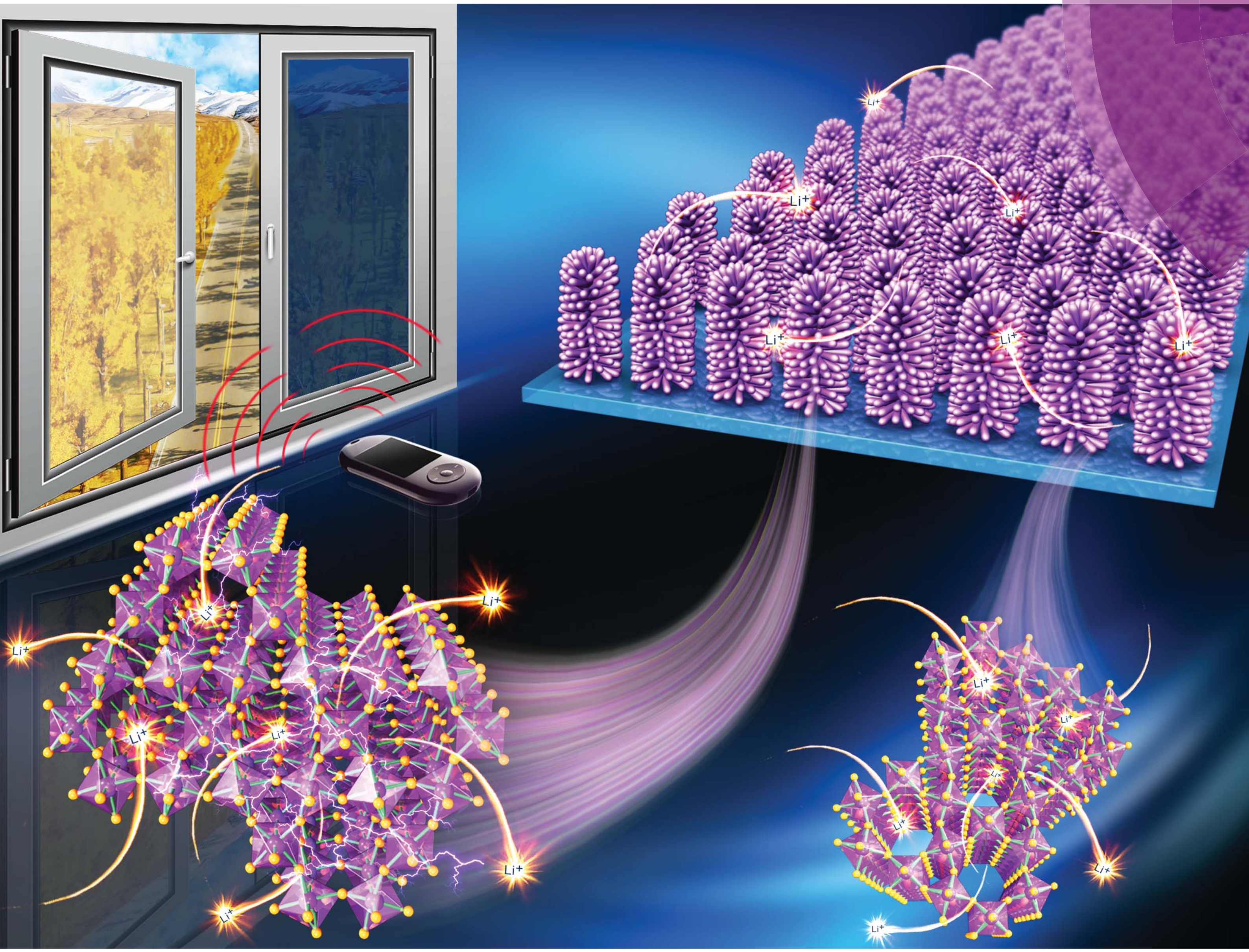

ISSN 2050-7488

ROYAL SOCIETY OF CHEMISTRY | Celebrating IYPT 2019

PAPER
Chunyang Jia *et al.*
Directly grown high-performance WO_3 films by a novel one-step hydrothermal method with significantly improved stability for electrochromic applications

Journal of
Materials Chemistry A

ROYAL SOCIETY
OF CHEMISTRY

PAPER

View Article Online
View Journal | View Issue

Check for updates

Cite this: *J. Mater. Chem. A*, 2019, 7, 13956

Directly grown high-performance WO_3 films by a novel one-step hydrothermal method with significantly improved stability for electrochromic applications†

Jianbo Pan, Yi Wang, Rongzhong Zheng, Maotong Wang, Zhongquan Wan, Chunyang Jia,* Xiaolong Weng, Jianliang Xie and Longjiang Deng

Received 2nd February 2019
Accepted 5th April 2019

DOI: 10.1039/c9ta01333d

rsc.li/materials-a

Currently, the electrochromic technology is still facing problems of high-cost and inadequate electrochromic performance. The WO_3 film prepared by the conventional hydrothermal method usually needs a crystal seed layer to be prepared on the substrate, which incurs additional energy consumption and retards electron transport. This paper presents a novel idea of a one-step hydrothermal synthesis combining the self-seeded agent glycerol with the capping agent ammonium sulfate ($(NH_4)_2SO_4$), which avoids the need for a complex preparation process and significantly enhances cyclic stability. Under the synergistic effect of the glycerol and $(NH_4)_2SO_4$, the resultant hexagonal system WO_3 (hex-WO_3) film exhibited a novel "coral-like" nanostructure and showed excellent electrochromic properties: a fast switching time (6/5 s for bleaching/coloration), a good coloration efficiency (56.5 cm^2 C^{-1}), and a large optical modulation (~78.1%) at 630 nm by applying ±1 V voltages. More importantly, the film obtained an outstanding cyclic stability (15 000 cycles without significant decay). Additionally, an electrochromic device (ECD) was successfully assembled, exhibiting fascinating performances, in which Prussian blue (iron(III) hexacyanoferrate(II), PB) was used as a complementary electrode.

Introduction

Electrochromism is a phenomenon whereby the optical properties (reflectivity,[1] absorptivity,[2] transmittance[3]) of materials change steadily and reversibly with an applied electric field. In terms of appearance, electrochromic materials show reversible changes of color and transparency. Therefore, electrochromic materials exhibit high practical application value, including in energy efficiency windows,[3,4] electrochromic display devices,[5,6] no glare automobile rear-view mirrors,[7] and so on.[8,9] In the field of electrochromism, WO_3 is one of the most widely studied electrochromic materials due to its characteristics of a high coloring efficiency, large contrast ratio, and good cycling stability.[10] The WO_3 electrochromic film can achieve a mutual transformation from colorless to deep blue by the intercalation/de-intercalation of cation ions (H^+, Li^+, Na^+, K^+)[11,12] and electrons. Moreover, in infrared wavelength, the WO_3 film also displays good electrochromic performance, which enables WO_3-based ECDs to achieve higher promise in applications for energy-saving buildings.[13–15]

Recently, the hydrothermal technology used to synthesize tungsten oxide crystal has attracted wide attention due to its low-energy consumption, simple preparation equipment, and as no special environment is required.[16,17] In the hydrothermal process, WO_3 films with different nanostructures[16,18–21] can be accurately and easily obtained by controlling the reaction concentration, temperature, and time,[22] pH value,[23,24] or by choosing different capping agents.[25] Nevertheless, because WO_3 has a relatively high lattice mismatch with FTO,[26] growing a WO_3 film by the hydrothermal method usually requires a crystal seed layer on FTO-coated glass to be prepared utilizing spin coating and sintering technology (~400 °C), which incurs extra energy costs and limits its commercial production. More importantly, grain boundaries, existing in the nanocrystalline seed layer, can retard electron transport.[27] Hitherto, only a few research studies about the use of self-seeded hydrothermal technology to synthesize a WO_3 film on FTO-coated glass have been performed.[27–30] These works have indicated that a WO_3 film can directly grow on FTO-coated glass with hydrogen bonding forces and some physical adsorption forces. However, all of the WO_3 films prepared this way display relatively poor cyclic stability (only a few thousand cycles). Hence, there is a pressing need to develop a facile and low energy-cost strategy

---

State Key Laboratory of Electronic Thin Films and Integrated Devices, National Engineering Research Center of Electromagnetic Radiation Control Materials, School of Electronic Science and Engineering, University of Electronic Science and Technology of China, Chengdu 610054, P. R. China. E-mail: cyjia@uestc.edu.cn; Fax: +86 28 83202569; Tel: +86 28 83201991

† Electronic supplementary information (ESI) available. See DOI: 10.1039/c9ta01333d

to prepare high-performance WO_3 electrochromic films, but this remains challenging.

Glycerol with three hydroxyl (–OH) groups and a short chain structure is a promising self-seeded agent that can improve the adhesion of a film with FTO-coated glass, but it hasn't been reported to date. One possible reason for this is given by Qi Ji and co-workers,[31] who researched the effects of different molecules on crystal growth, and found that the number of –OH groups could affect the growth of oxide crystals and that molecules with three –OH groups would cause the crystal to grow and stack in a three-dimensional (3D) direction. Thus, glycerol can make the WO_3 film obtain a compact stacking structure, which is very bad for ion transport. Fortunately, it is easy to control the crystal growth trend under hydrothermal conditions by choosing different capping agents, such as urea,[32] oxalic acid,[33] and sodium sulfate,[20] which makes it clear that choosing the appropriate capping agent to improve the crystal structure of the film affected by polyhydroxy molecules is a hopeful strategy.

In this work, hex-WO_3 films were directly synthesized on FTO-coated glass by a novel low-temperature (120 °C) glycerol-assisted hydrothermal method, in which $(NH_4)_2SO_4$ served as a capping agent to further control the crystal growth efficiently. The resultant hex-WO_3 film exhibited a novel coral-like nanostructure and outstanding cyclic stability, which indicated that there was a strong adhesion between WO_3 films and FTO. Simultaneously, the film also showed broad optical modulation, a fast switching speed, and good coloration efficiency. For a deeper understanding, we explored the synergistic mechanism of a self-seeded agent and capping agent on film growth and on the electrochemical and electrochromic properties. Finally, an assembled ECD exhibited excellent electrochromic performances, which demonstrated the application potential of the prepared WO_3 film in the ECD field.

Results and discussion

Crystal structure

According to reports,[18,25,34] the amount of capping agent is an important factor for crystal growth. In this work, glycerol with a constant mass was designed to explore the self-seeded growth phenomenon of a WO_3 film on FTO-coated glass. Meanwhile, a quantitative research method, which is an important experimental means, was used to discuss the effect of different amounts of $(NH_4)_2SO_4$ on crystal growth. In hydrothermal solution, the stoichiometry of the $(NH_4)_2SO_4$ and tungsten atoms was controlled to 0 : 1, 2 : 1, 4 : 1, 6 : 1, and each of the films was denoted as W-AS0 (0 mmol), W-AS2 (2.1 mmol), W-AS4 (4.2 mmol), W-AS6 (6.3 mmol). Also, crystal seed layer assisted film prepared under the same conditions as the W-AS4 film was denoted as W-AS4_seed. Additionally, the sample prepared with only de-ionized water without glycerol and $(NH_4)_2SO_4$ was denoted as the pure-H_2O sample. The detailed experimental preparation process is explained in the Experiment part.

To determine the crystal structure and possible phase changes in different hydrothermal conditions, XRD patterns for the FTO-coated glass with and without WO_3 films are shown in Fig. 1a. The XRD diffraction peaks of the blank FTO-coated glass clearly correspond to JCPDS no. 41-1445, and were found at the same positions in all films, marked here as "▽" in order to distinguish them. The XRD pattern of the W-AS0 film could be indexed to orthorhombic $WO_3 \cdot 0.33H_2O$ (ort-$WO_3 \cdot 0.33H_2O$) on JCPDS no. 87-1203. With the addition of $(NH_4)_2SO_4$, the XRD patterns of W-AS2, W-AS4, and W-AS6 films correspond to JCPDS no. 85-2459, which verifies that hex-WO_3 was obtained. Nevertheless, for the W-AS6 film, the XRD peaks' diffraction intensity are clearly very low. Under hydrothermal conditions where $(NH_4)_2SO_4$ exists, the SO_4^{2-} ions can be absorbed on the faces parallel to the *c*-axis, which can form strong energy barriers to control crystal growth along the [001] face.[16,25,35] Meanwhile, as the crystal grows, NH_4^+ ions can be inserted into the ion tunnels of hex-WO_3 crystal, which makes the growth ability of the [001] face stronger than that of the other faces.[34] Therefore, under the mutual action of SO_4^{2-} and NH_4^+ ions, the XRD peaks' diffraction intensity of the (002) crystal face in the prepared hex-WO_3 films is enhanced, which demonstrates the action of $(NH_4)_2SO_4$ controlling the crystal growth in the glycerol-assisted hydrothermal process. However, superfluous SO_4^{2-} ions absorption is unfavorable for crystal growth as it induces poor crystallinity for the W-AS6 film. Moreover, excessive $(NH_4)_2SO_4$ can also make the energy of growth on the (100) and (001) faces comparable, resulting in a greatly weakened anisotropic growth of the WO_3 crystal.[34]

The ort-$WO_3 \cdot 0.33H_2O$ phase is very sensitive to the preparation condition, which can be synthesized at a hydrothermal temperature of 120 °C.[27,30,36] Some studies[20,36,37] revealed the crystal structure of ort-$WO_3 \cdot 0.33H_2O$, which consists of two types of corner-sharing WO_6 octahedra (Fig. 1b). Type I includes six oxygen atoms surrounding the central tungsten atom and can connect six different octahedra through corner-sharing; while in type II, two of the oxygen atoms are replaced by a shorter terminal W=O bond and a longer W–$(OH)_2$ bond, respectively. It is impossible for these oxygen atoms to bond to other W atoms covalently. Therefore, for the ort-$WO_3 \cdot 0.33H_2O$ crystal, the upper and lower layers can only be bonded by dislocation, which leads to a relatively weaker interaction between adjacent layers.[20,36]

The NH^{4+} ions play a vital role in constructing hex-WO_3 nanostructures with the addition of $(NH_4)_2SO_4$.[34,38–42] The crystal structure of hex-WO_3 (Fig. 1b) consists of only type I octahedra, whose corner-sharing oxygen can be bonded not only in the *c*-axis direction but also in the *ab*-plane, which is very different from ort-$WO_3 \cdot 0.33H_2O$.[43] Through the connection of these WO_6 octahedra, a hexagonal window and trigonal cavity can be formed in the *c*-axis direction, constituted by six-membered rings and three-membered rings, respectively. Meanwhile, a four-coordinated square window can also be found in the *ab*-plane direction.[43–47] All of these structures in hex-WO_3 can act as tunnels to transport Li^+ ions. Because the Li^+ ion has a small ionic radius, it can be accommodated by the trigonal cavity after transporting through the hexagonal window and four-coordinated square window. Moreover, for the deintercalation process, the Li^+ ion also has an ordering phenomenon from the trigonal cavity to the four-coordinated square window, to the

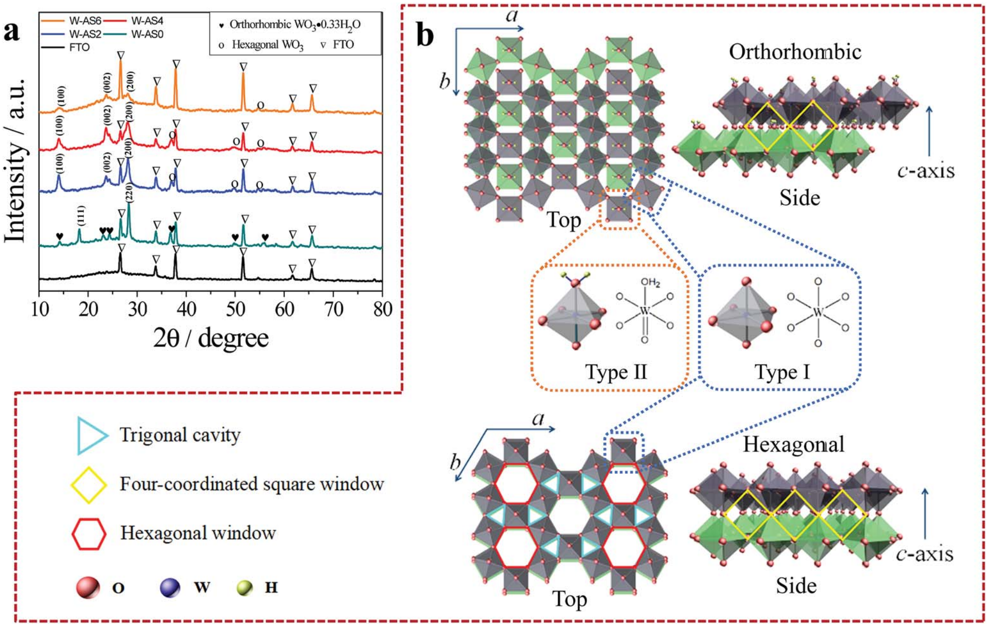

Fig. 1 (a) XRD patterns for FTO-coated glass and WO_3 films with different amounts of $(NH_4)_2SO_4$; (b) schematic illustration of the orthorhombic $WO_3\cdot0.33H_2O$ and hexagonal WO_3 crystal structures: top and side view of the crystal structure, octahedra of type I and type II.

hexagonal window, and then extracted from the WO_3 crystal.[43,45] However, for the ort-$WO_3\cdot0.33H_2O$ crystal, the dislocation arrangement of each layer results in a relatively small number of tunnels. Therefore, hex-WO_3 with more ion tunnels and an orderly ion transport process make it easier to transport Li^+ ions than in the case of ort-$WO_3\cdot0.33H_2O$, which was reflected in the subsequent electrochemical tests.

Thus, it can be known that under the glycerol-assisted hydrothermal condition, $(NH_4)_2SO_4$ contributes to controlling the anisotropic growth of the crystal and the formation of the hexagonal structure, which are favorable for performance improvement.

Formation mechanism

In order to understand the self-seeded growth mechanism, the pertinent synthesis processes for hex-WO_3 and ort-$WO_3\cdot0.33H_2O$ crystals are discussed in the ESI (Scheme S1†). The polycondensation precursor monomers of the WO_3 crystal have –OH groups, and thereby other –OH and carboxylic (–COOH) groups can connect with the crystal nucleus by forming a hydrogen bond.[48–50] Moreover, the surface of the FTO-coated glass, which was characterized by Fourier transform infrared (FT-IR) spectroscopy (Fig. S1†), was active and rich in –OH groups. Therefore, as shown in the schematic diagram of Fig. 2f, glycerol possibly served as a bridge to connect the WO_3 crystal nucleus with FTO. Owing to the formation of hydrogen bonding force and other physical adsorption effects, the WO_3 film could be effectively attached to the FTO-coated glass. As shown in Fig. S2,† it was confirmed *via* a simple grid-sticking method that glycerol could strengthen the adhesive force between the WO_3 film and FTO.

Fig. 2a–e show SEM images of the resultant WO_3 films, which can aid understanding the action of glycerol and $(NH_4)_2SO_4$ in the film growth. Because the pure-H_2O film is an orthorhombic crystal system (Fig. S3†) and the crystal was grown under free conditions without interference from molecules or ions, its nanostructure (Fig. 2a) shows a "brick" shape. When the glycerol takes part in the hydrothermal reaction, irregular lamellar structures appear and stack into 'spindle-like' nanostructures because of the hydrogen bond action and the increase in the hydrothermal solution viscosity. The lamellar crystals with larger area are more likely to bond to other lamellar crystals, which results in them being in the middle of the spindle-like nanocrystals. With the addition of $(NH_4)_2SO_4$, the crystal type changes from an orthorhombic crystal system to a hexagonal crystal system, and the crystal H_2O is simultaneously lost. In the hexagonal crystal system, SO_4^{2-} ions are used as a capping agent to form nanorods.[16,25,35] The nanorods of the W-AS2 film self-assemble into a small sheet shape, possibly due to the formation of hydrogen bonding by glycerol under high-pressure conditions. For W-AS4 film, the effect of glycerol on the nanorods is dramatically reduced due to the greater SO_4^{2-} ions adsorption, which leads to one end of the nanorods gathering together and forming a coral-like nanostructure. The formation of compact nanospheres in the W-AS6 film indicates poor crystallinity, which was similar to the result from the XRD characterization. For a clearer understanding, simple schematic diagrams of crystal growth with different types and different quantities of additives are shown in Fig. 2f. Moreover, the cross-sectional SEM images are shown in Fig. S4,† which exhibits the undulating morphology of the WO_3 films. The thickness of the W-AS0, W-AS2, W-AS4, and W-AS6 films were about 1.11 μm, 1.88 μm, 1.58 μm, and 0.81 μm, respectively.

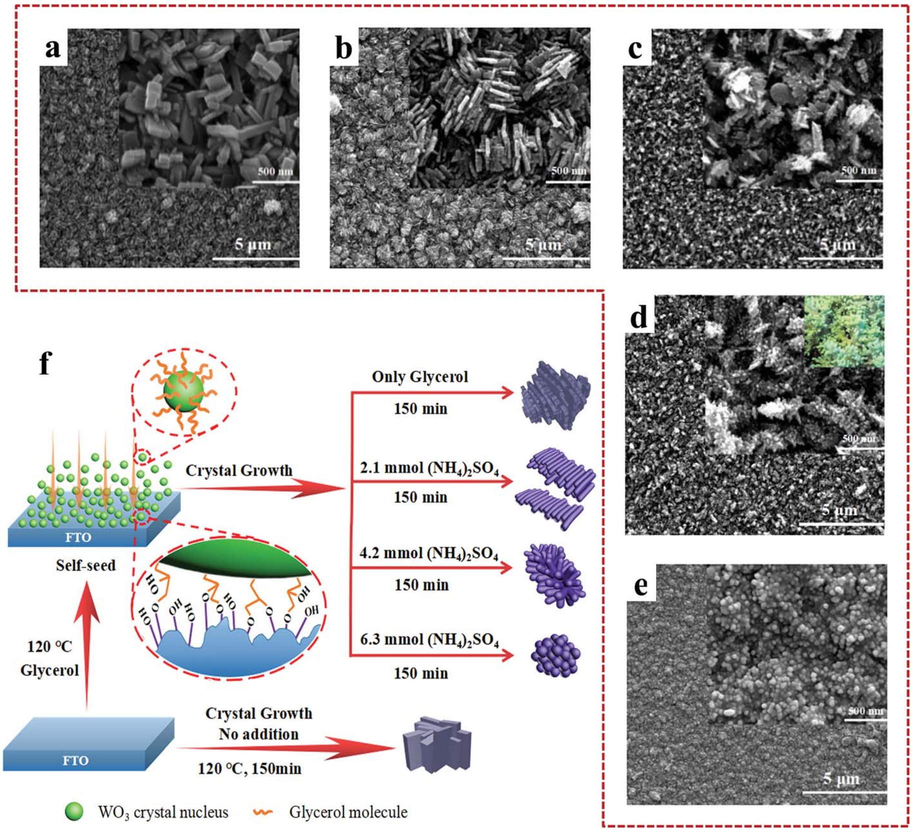

Fig. 2 SEM images of WO_3 films, while the insets show high-magnification images: (a) pure-H_2O, (b) W-AS0, (c) W-AS2, (d) W-AS4, and the small inset shows the real coral photo, (e) W-AS6; (f) schematic illustration of the process of glycerol self-seeded growth, and the nanostructure of WO_3 films with different types and different quantities of additives.

The W-AS4 film obtained the best crystallinity of the hexagonal crystal and displayed a novel coral-like nanostructure, while its dendritic structure can supply more redox reaction sites. The outstanding performance of the W-AS4 film is discussed later in the electrochemical and electrochromic analysis. W-AS4 films were grown at different times in order to explore the growth process, with their SEM images and XRD patterns shown in Fig. 3a–e, respectively. The characterizations manifest the approximate process of self-seeded and crystal growth control. Here, a crystal seed layer was first formed after 30 min hydrothermal reaction, which was proved to be amorphous by the XRD pattern. Second, when the time reached 70 min, the film obtained a low crystallinity, which confirmed that the crystal had begun to grow. After that, the WO_3 crystal gradually grew and the short nanorods clustered into irregular rod-like shapes at 110 min. When the hydrothermal reaction proceeded for 150 min, the coral-like nanostructure with a good crystallinity was obtained, for which the TEM images are shown in Fig. 4c and d. As exhibited in the low-magnification image, it can be seen that the coral-like nanostructures were formed through the gathering of one end of the nanorods with diameters of about 10 nm. The HRTEM image of the nanorods confirmed the spacing of the lattice fringes to be 0.383 nm, which correspond to the (002) lattice planes of hex-WO_3 (JCPDS no. 85-2459). Thus, these short nanorods formed after hydrothermal reaction for 110 min and gradually grew along the [001] crystal plane, forming the dendrites of the coral-like nanostructure under the effect of SO_4^{2-} and NH_4^+ ions. Additionally, the TEM images of W-AS0 powder are shown in Fig. 4a and b. In the HRTEM image of the spindle-like nanocrystals, the lattice fringes at 0.369 nm and 0.318 nm correspond to the (200) and (040) crystal planes of ort-$WO_3 \cdot 0.33H_2O$ (JCPDS no. 87-1203), respectively. Therefore, this can further distinguish the ort-$WO_3 \cdot 0.33H_2O$ from the hex-WO_3 crystals.

As discussed above, glycerol can make the WO_3 film directly grow on FTO-coated glass but a good crystallinity can only be got by adding the proper amount of $(NH_4)_2SO_4$. Moreover, it takes 150 min to form the coral-like nanostructure. Accordingly, the adverse effect of glycerol on crystal growth has been successfully avoided, and a fluffy and porous morphology is formed, which could prove the notion that directly growing WO_3 film by the synergistic effect of self-seeded and capping agents is a feasible strategy.

Comparative analysis of electrochemical properties

Cyclic voltammetry (CV) tests were carried out between −1.0 V and +1.0 V at a scan rate of 50 mV s^{-1}. The results are shown in Fig. 5a, including the CV curves of the W-AS0, W-AS2, W-AS4, W-AS6, and W-AS4_seed films. The areas of the CV hysteresis curves increases with the moderate addition of $(NH_4)_2SO_4$,

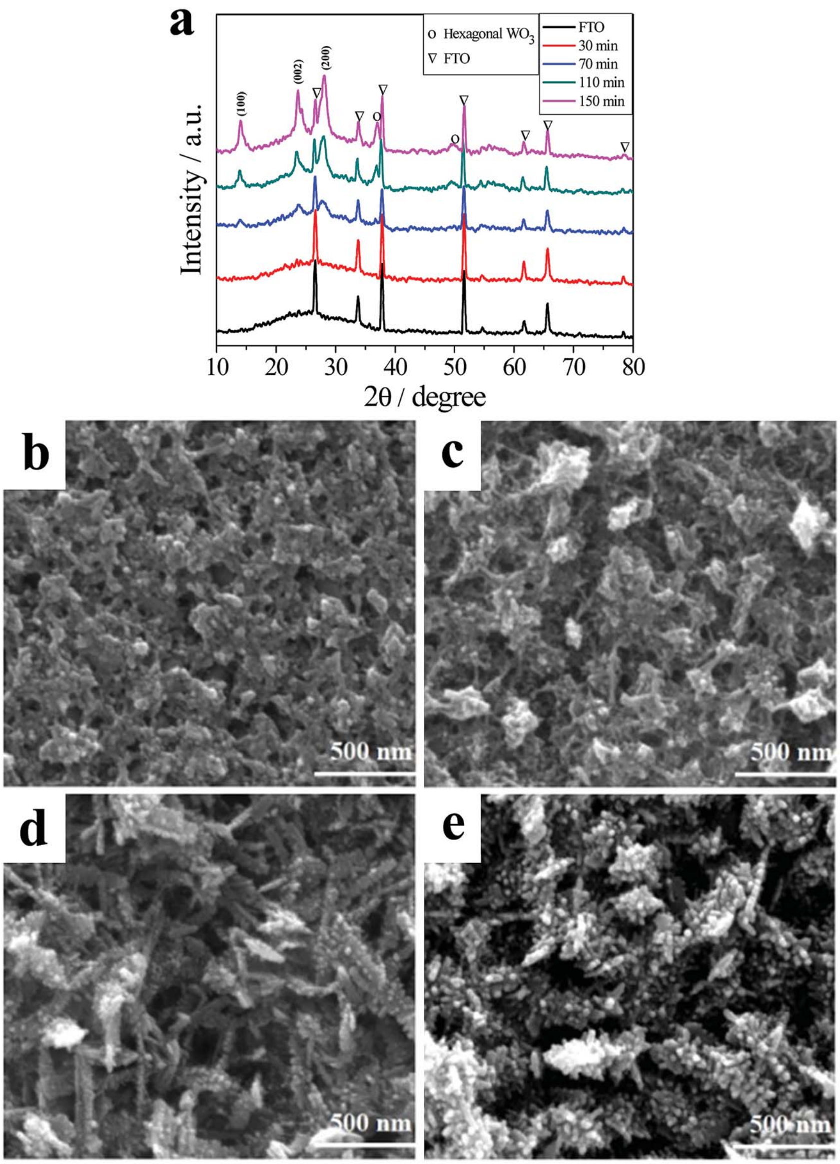

Fig. 3 (a) XRD patterns for FTO-coated glass and W-AS4 films with different growth times; SEM images of W-AS4 films on FTO-coated glass with different growth times: (b) 30 min, (c) 70 min, (d) 110 min, (e) 150 min.

which proves that more Li^+ ions can intercalate/de-intercalate from the film, especially in the W-AS4 film. Furthermore, the onset potential of the cathodic current for the W-AS4 film was strongly shifted in a positive direction when compared with the other films, that is to say, Li^+-ion insertion can be achieved at a relatively low applied voltage.[51] It was shown from the XRD and SEM analyses that under the effect of an appropriate addition amount of $(NH_4)_2SO_4$, the hexagonal structure with the porous coral-like nanostructure is formed. Moreover, the specific surface area of each structure was tested by nitrogen (77 K) adsorption and the results are shown in Table S3.† It should be noted that due to the low yields of W-AS6 powder with low crystallinity, the surface area could not be tested. It was found that the specific surface area of the W-AS4 structures was 22.5 $m^2\ g^{-1}$. Clearly, the specific surface area of the W-AS4 structure was bigger than for the other structures (10.1 $m^2\ g^{-1}$ for W-AS0, 10.3 $m^2\ g^{-1}$ for W-AS2), which means it can contribute more active sites for oxidation–reduction reactions.[52] The process of Li^+-ions intercalation/de-intercalation is roughly divided into three steps: (1) the electrolyte solution infiltrates into the film; (2) the ions are transported in the film; (3) the ions intercalate/de-intercalate from the crystal through the lattice tunnels. Both (1) and (2) are attributed to the porous nanostructure of the film, while the last one is determined by the crystal structure and crystallinity. Therefore, the W-AS4 film is dominant in all of these three steps, because it has the most ideal hexagonal crystal structure and coral-like nanostructure which can provide more active sites for the redox reactions compared with the other films, resulting in more efficient Li^+-ion mobility.

It was found that there are two pairs of redox peaks in the CV curves of WO_3 films, which is attributed to the two main types of ion-injection sites: active sites (reversible) and trap sites

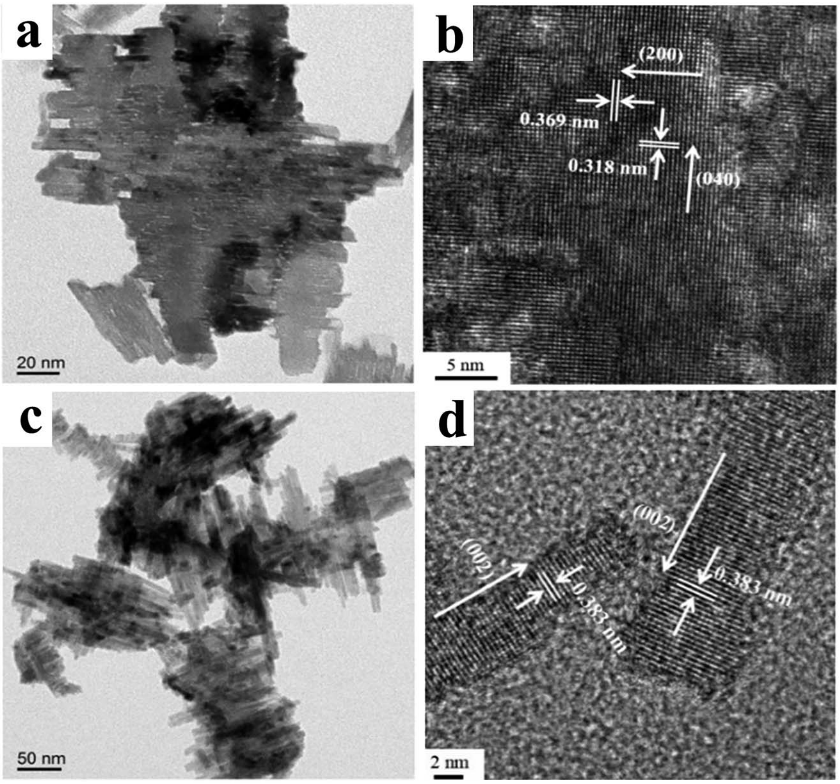

Fig. 4 TEM images of W-AS0 powder: (a) low-magnification image, (b) HRTEM image; TEM images of W-AS4 powder: (c) low-magnification image, (d) HRTEM image.

(reversible to shallow traps and irreversible to deep traps).[53–55] In addition, with the appropriate increase in $(NH_4)_2SO_4$ content, the potentials of the oxidation peak shift in the positive direction and become broadened, but the peak-current of the W-AS0 film is bigger than that of the W-AS2 film. The same phenomenon has also been reported in other works,[29,56,57] and the reason for it can be that W-AS2 film contains a higher amount of redox centers, which are more distant from the FTO layer and thus have a different electrochemical neighborhood.[57] However, for the W-AS4 film, the above influence is weakened due to the ordered ion-transport tunnels and more active reaction sites, thus it exhibited the largest current densities (high exchanged charge densities) compared with the other films.

To further understand the charge transfer and Li^+-ion mobility of the as-prepared WO_3 films during the electrochemical process, EIS measurements were conducted in three-electrode systems with an AC voltage of 5 mV in a frequency range of 0.01 Hz to 100 kHz in their bleached state. Fig. 5b shows the EIS results, which consist of semicircles in the high-frequency region and straight lines in the low-frequency region, respectively. Generally, a larger semicircle means a larger charge-transfer resistance, and a lower slope is related to a higher ion-diffusion resistance.[58] Compared with the other

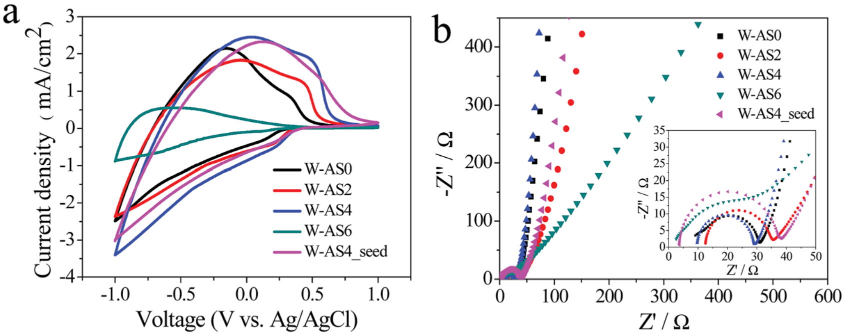

Fig. 5 (a) CV curves of WO_3 films synthesized under different hydrothermal conditions; (b) electrochemical impedance spectroscopy (EIS) results (inset: high-frequency region) of WO_3 films synthesized under different hydrothermal conditions.

films, the W-AS4 film had a smaller semicircle radius at high frequency and a higher slope at low frequency (Fig. 5b), indicating that the W-AS4 film achieves a lower charger-transfer resistance and faster ion-transport rate, which was the same as the CV analysis results. It is worth noting that the W-AS4_seed film had a relatively larger semicircle than the W-AS4 film in the low-frequency region, and lower anodic and cathodic current peaks in the CV curve, which confirmed the retardation effect of the crystal seed layer on electronic transport.

Step chronoamperometric cyclic tests were used to compare the stability of the films, and the results are shown in Fig. S6a–d.† The W-AS6 film showed the worst stability compared with the other films and began to drop sharply after 100 cycles, which was due to the poor crystallinity.[59–61] Stemming from the ort-$WO_3 \cdot 0.33H_2O$ crystal structure and dense spindle-like morphology, the current in the W-AS0 film began to drastically reduce after about 300 cycles. In addition, both the W-AS0 and W-AS6 films shed current after hundreds of cycles, which was likely a consequence of the sharp volumetric change of the WO_3 crystal and increased stress during the process of Li^+-ions intercalation/de-intercalation.[62] However, the W-AS2 and W-AS4 films still maintained good performance after 1000 cycles, but the current in the W-AS2 film gradually decreased with the increasing number of cycles. Different from the W-AS2 film, the current in the W-AS4 film gradually increased over 1000 cycles, indicating that the W-AS4 film was still in the activation stage within at least 1000 cycles, which could be attributed to its large accessible surface area and multi ion tunnels crystal structure, which makes it able to accommodate more Li^+ ions and to bear the impact stress from the ions. The step chronoamperometric cyclic test of W-AS4_seed film is given in Fig. S8,† which indicates that the W-AS4_seed film has a similar activation stage in 1000 cycles.

Electrochromic properties of W-AS4 film

As in the above investigation, the W-AS0, W-AS2, and W-AS6 films showed relatively poor electrochemical stability performances because their nanostructures had less robustness during the electrochemical process. For this reason, only the W-AS4 film and W-AS4_seed film were selected to further investigate the electrochromic properties. The electrochromic properties were measured after the film electrodes had been subjected to CV testing for 10 cycles. Fig. 6a displays the transmittance spectra of the W-AS4 film in colored and bleached states at wavelengths from 350 nm to 1100 nm, with −1.0 V and +1.0 V applied for 25 s, respectively. The color of the W-AS4 film changed from transparent (bleached state) to dark blue (colored state) reversibly. This process is in accordance with intercalation (de-intercalation) of the Li^+ ions and electrons into (out from) the WO_3 films:

$$\underset{\text{(transparent)}}{WO_3} + xLi^+ + xe^- \rightleftharpoons \underset{\text{(deep blue)}}{Li_xWO_3}$$

At 630 nm wavelength, the W-AS4 film exhibited a huge transmittance variation (ΔT) of ~78.1% at ±1.0 V voltage, which is better than reported in most works using the hydrothermal method (see Table 1). Fig. 6e presents the digital photographs of the W-AS4 film at different voltages. By polarization at different voltages, the film achieved a uniform color change (Fig. 6e). In particular, when a −2.0 V voltage was applied to the film, its color was almost black, while a +2.0 V voltage made the colored film turn back to its initial transparent state. Additionally, the electrochromic performance of the W-AS4_seed film is given in Fig. S9,† and could be compared with the W-AS4 film.

The switching time is an important factor to evaluate the EC property, and is usually defined as the time required for a device to reach 90% of full optical modulation. Step voltages of +1.0 V and −1.0 V were applied to the bleached and colored processes, respectively. Fig. 6b presents the relationship between the time and transmittance variation at 630 nm wavelength, and the coloration time (t_c) was 5 s, while the bleaching time (t_b) was 6 s. Because of the ideal hexagonal crystal structure and porous morphology, the W-AS4 film obtained a fast switching speed, which was comparable with other WO_3 films obtained using crystal-seed-assisted or self-crystal-seeded hydrothermal methods (as shown in Table 1).

The coloration efficiency (CE) is a characteristic parameter for evaluating the electrochromic property and is defined as the change in optical change (ΔOD) at a specific wavelength per unit charge density (ΔQ) in the coloring process. This parameter can be calculated using the following eqn (1):[63]

$$CE = \Delta OD/\Delta Q = \log(T_b/T_c)/\Delta Q \tag{1}$$

where T_b and T_c refer to the bleached and colored transmittance values at a special wavelength, respectively. Fig. 6c shows the ΔOD value at a wavelength of 630 nm *versus* the inserted charge density at −1.0 V. With increasing the ΔQ, the ΔOD value reached ~1.8 when the coloring process reached a steady state, which disclosed that the W-AS4 film could achieve a deep coloration with charge injection. The CE value for the W-AS4 film was 56.5 $cm^2\ C^{-1}$ by calculation using eqn (1).

The cyclic stability of the electrochromic film is a crucial factor currently limiting the future practical application of electrochromic materials. It can be seen from Fig. 6d that the W-AS4 film was still in an active state for about 3000 cycles (maximum increase by ~4.9% compared with the initial stage). Some similar examples of the phenomenon of the electrochemical activation process can also be found in other works.[64–68] The reason for this phenomenon can be attributed to the removal of NH_4^+ ions from the WO_3 crystal lattice, which allows more Li^+ ions to participate in the electrochemical reaction. However, further research is needed to prove this guess. After the active stage, the optical modulation performance of the W-AS4 film reached a stable state. By prolonging the number of cycles to 15 000, the ΔT of the film maintained a large value (~78.9%) without any significant decay. To the best of our knowledge, few works have reported WO_3 electrochromic films prepared by hydrothermal techniques able to achieve such a high cycle stability. Some comparisons with other reports are shown in Table 1. The possible reasons for the fascinating cyclic stability are as follow: (1) the three –OH groups and short chain

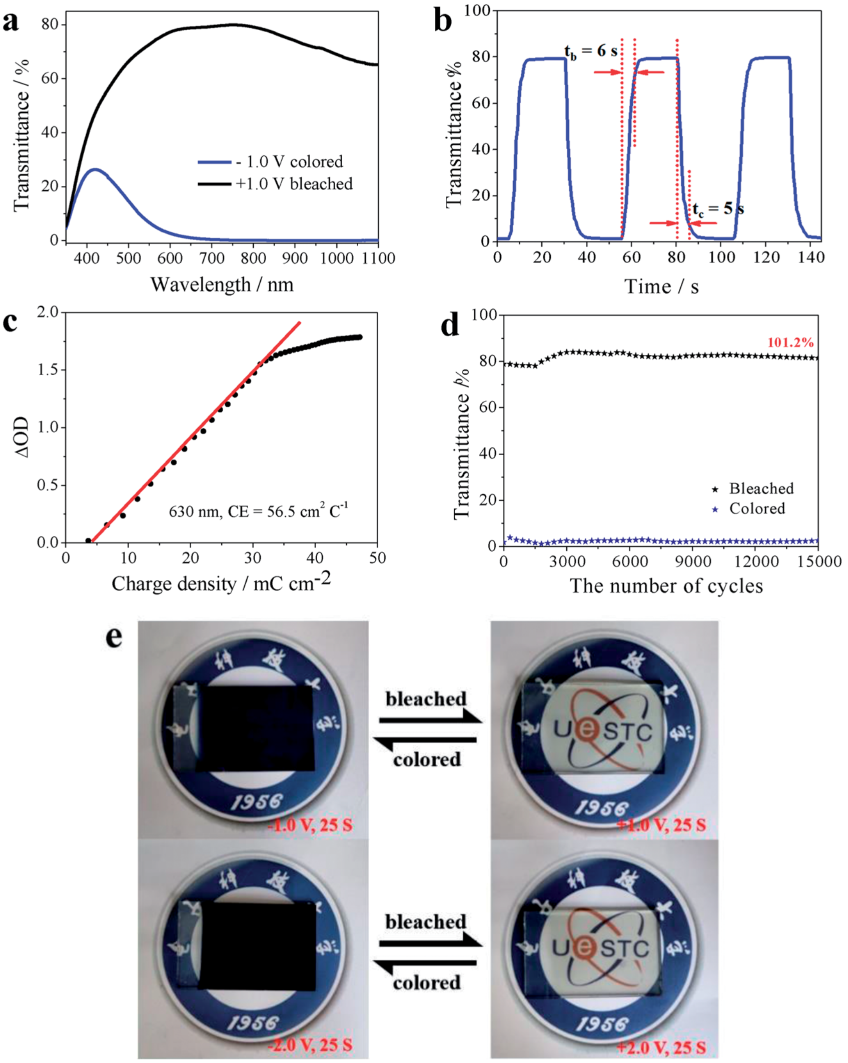

Fig. 6 (a) UV-vis transmittance spectrum of the W-AS4 film in colored and bleached states between 350 nm and 1100 nm; (b) switching time and transmittance variation curves between colored and bleached states at 630 nm, ±1.0 V bias; (c) variation of the optical density (ΔOD) *versus* charger density (*Q*) of the W-AS4 film; (d) cyclic stability test of the W-AS4 film for coloration and bleaching at 630 nm, ±1.0 V; (e) digital photographs of the W-AS4 film at different states.

structure of glycerol make the WO_3 film adhere to the FTO firmly; (2) during the process of Li^+-ions intercalation/de-intercalation, the coral-like nanostructure of the W-AS4 film can endure the expansion/contraction deformation of the film and the impact stress efficiently, which is attributed to its fluffy porous morphology and the possible interlocking force between dendrites (as shown in Fig. S10†); (3) the hexagonal crystal structure of the W-AS4 film provides many ordered ion channels to facilitate the ions being transported efficiently.

To sum up, the electrochromic behavior of the WO_3 film is correlated with its crystal structure and nanomorphology.[18] For the W-AS4 film, the hexagonal windows, four-coordinated square windows, and trigonal cavities existing in the hexagonal crystal structure can act as Li^+-ion transport tunnels, which leads to a large ion-diffusion coefficient. Meanwhile, the porous coral-like nanostructures efficiently promote the insertion and extraction of Li^+ ions from the film. Therefore, the W-AS4 film possesses a large number of active sites for electrochemical reactions and a sufficient number of Li^+ ions can be used as electrochemical reaction substances, which indicates the strategy of combining a capping agent with a polyhydroxy self-seeded agent used to directly grow WO_3 film could achieve ideal results.

Performance of ECD

In order to further investigate the application of the W-AS4 film in ECD, a prototype device consisting of a W-AS4 film working electrode, PB film ion storage layer, and 1 M $LiClO_4$/PC electrolyte was assembled. The PB film was chosen as an ion storage layer due to its complementarity with the WO_3 electrochromic material, and its electrochemical properties are presented in Fig. S11.† Fig. 7a and b show the UV-vis transmittance spectrum and a digital photograph of the device, respectively. When

Table 1 Partial list of references on the properties of hydrothermal-based WO_3 electrochromic films ($LiClO_4$/PC electrolyte)

Hyd[a] [°C h^{-1}]	Ann[b] [°C h^{-1}]	V_c/V_b[c] [V]	ΔT/Wl[d] [%/nm]	T_c/T_b [s]	Cyclic stability	Ref.
120/2.5	—	−1.0/+1.0	78.1/630.0	5.0/6.0	After 15 000 cycles without significant decay of ΔT	This work
120/2.0	—	−3.0/+3.0	30.0/632.8	26.0/5.5	After 1000 cycles without significant decay of PKC[e]	27
120/2.0	400/2.0	−0.57/+0.64	64.7/630.0	1.0/1.0	After 5000 cycles without significant decay of CV current	30
180/18.0	—	−0.8/+0.8	45.0/754.0	7.9/4.8	After 2000 cycles without significant decay of CV current	29
180/4.0	—	−2.0/+2.0	58.0/633.0	7.6/4.2	After 500 cycles without significant decay of ΔT	16
180/12.0	—	−3.0/+3.0	68.0/632.8	9.3/5.7	After 500 cycles without significant decay of ΔT	10
180/12.0	—	−2.0/+2.0	66.0/632.8	6.7/3.4	After 1000 cycles without significant decay of CV current	18
180/3.0	—	−1.5/+1.0	86.0/600.0	19.0/6.2	ΔT remaining was 86.8% after 5500 cycles	61

[a] Hyd: hydrothermal technology. [b] Ann: annealing technology. [c] V_c/V_b: the voltage of coloring and bleaching. [d] ΔT/Wl: the transmittance variation of colored and bleached states, the wavelength of optical modulation. [e] PKC: the peak current of colored and bleached states.

applying voltages of −1.0 V, −2.0 V, and −3.0 V, the device displayed a uniform color change from transparent to deep blue and a large optical modulation range from 350 nm to 1100 nm wavelength. The switching time and transmittance variation curve are shown in Fig. 7c, in which the ECD exhibited a large ΔT of ~77.8% and a short switching time (14/5 s for bleaching/coloration) at 630 nm. It is noteworthy that the ECD had a relatively low bleaching speed, which was different from the W-AS4 film. As is well known, both the electrochromic layer and ion storage layer can affect the switching speed of the ECD. As shown in Fig. S11,† the bleaching time (6 s) of PB was longer than the coloring time (2.5 s), which led to a relatively slow oxidation–reduction reaction speed for the ECD in the bleaching process. By calculating the ΔOD and ΔQ values, the ECD obtained a CE value of 213.9 cm^2 C^{-1}. Overall, this device exhibited outstanding electrochromic properties, which suggest the promising application of W-AS4 films in smart windows and other fields.

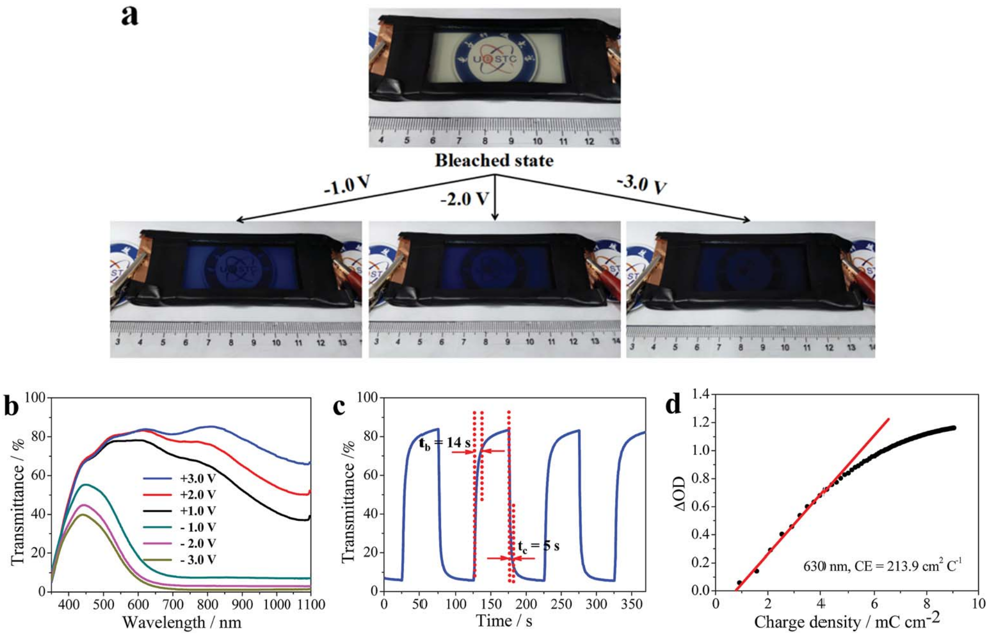

Fig. 7 The performance tests of the fabricated ECD (4.0 cm × 6.0 cm): (a) digital photograph in the colored and bleached states under different voltages; (b) UV-vis transmittance spectrum in the colored and bleached states under different voltages; (c) switching time and transmittance variation curve between the colored and bleached states at 630 nm, ±2.0 V, 50 s each stage; (d) variation of the optical density (ΔOD) *versus* the charge density (Q).

Conclusions

In summary, a novel idea is presented to simplify the hydrothermal procedure in preparing a WO_3 film to significantly improve its cyclic stability. It was found that using the synergistic-effect mechanism of glycerol and $(NH_4)_2SO_4$, a high-performance WO_3 film could be directly grown on a substrate under low-temperature hydrothermal conditions. *Via* optimized design, the resultant WO_3 film obtained a hexagonal crystal system and a novel coral-like nanostructure, and exhibited excellent electrochromic properties, and outstanding cyclic stability of 15 000 cycles without significant decay especially. Through performing characterizations, performance measurements, and comparison tests, the superior electrochromic properties were proved to be attributed to its ordered ion channels in a hexagonal crystal structure, porous coral-like morphology, and pretty good adhesion with FTO-coated glass. Meanwhile, the performance comparisons of W-AS4 film with and without a crystal-seed layer confirmed the retardation effects of crystal seed layer on electronic transport. Furthermore, the complementary ECD could change color from transparent to deep blue under ±2.0 V voltages, showing a fast switching speed and high coloration efficiency simultaneously. Therefore, the W-AS4 film for ECD application exhibited promising practical application prospects in energy-saving smart windows for architecture, automobiles, aircrafts, and so on.

Experimental

Materials

All the solvents and chemicals were of analytical grade and used without further purification. FTO-coated glass (7 Ω resistance, 2.2 mm thickness) was purchased from Wuhan lattice Solar Energy Technology Co., Ltd. Sodium tungstate ($Na_2WO_4\cdot 2H_2O$), ammonium sulphate ($(NH_4)_2SO_4$), hydrochloric acid (HCl, 36%), and hydrogen peroxide (H_2O_2, 30%) were purchased from Chengdu Kelong Reagent Co., Ltd. Anhydrous propylene carbonate (PC), glycerol, anhydrous lithium perchlorate ($LiClO_4$), potassium ferricyanide ($K_3[Fe(CN)_6]$), ferric chloride ($FeCl_3$), and potassium chloride (KCl) were purchased from Shanghai Aladdin Biochemical Polytron Technologies Inc.

Preparation of seed layer

The WO_3 seed solution was prepared according to the literature method.[27] Briefly, 1 g $Na_2WO_4\cdot 2H_2O$ powder was dissolved in 15 mL de-ionized water. 3 M HCl was added to the above solution until no more precipitate was formed. Afterward, the yellow precipitate was washed using de-ionized water in an ice bath and then the solution was centrifuged for 10 min at 8000 rpm. Finally, H_2O_2 (30%) was used to dissolve the washed precipitate and de-ionized water was added to make the concentration reach 0.2 M. The seed layer was coated on FTO-coated glass *via* a spin-coating technology, followed by annealing at 400 °C for 1 h.

Preparation of WO_3 film

The WO_3 films were synthesized on FTO-coated glass through hydrothermal technology. The procedure for preparing the precursor solution was reported in previous works.[30,69] Briefly, 3.29 g $Na_2WO_4\cdot 2H_2O$ powder was added in 30 mL de-ionized water and stirred for 5 min. 3 M HCl was added to the above solution until no more precipitate was formed. The yellow precipitate was washed using de-ionized water in ice bath several times and then the solution centrifuged for 10 min at 8000 rpm. Then, 4 mL H_2O_2 (30%) and the above precipitate were added to a beaker with a certain amount of de-ionized water to make the volume up to 100 mL. Finally, 0.1 M transparent homogeneous peroxopolytungstic acid solution was obtained after constant stirring and mild heating at 60 °C.

The WO_3 films were grown using peroxopolytungstic acid solution (0.1 M, 10.5 mL) with HCl (3 M, 3.5 mL), de-ionized water (20 mL), glycerol (24 mL), and a certain amount of $(NH_4)_2SO_4$. Then, a 30 mL mixture of above solutions was transferred to a 50 mL Teflon-line stainless-steel autoclave. The FTO-coated glass substrate (FTO-coated glass was washed with KOH ethanol solution, then de-ionized water, and finally with anhydrous ethanol in an ultrasonic bath for 20 min per wash) was placed vertically in the autoclave. Then, the autoclave was sealed and maintained at 120 °C for 2.5 h. The stoichiometry of $(NH_4)_2SO_4$ and tungsten atoms was controlled as 0 : 1, 2 : 1, 4 : 1, 6 : 1, with each of them denoted as W-AS0 (0 mmol), W-AS2 (2.1 mmol), W-AS4 (4.2 mmol), W-AS6 (6.3 mmol). Additionally, the crystal seed layer assisted film prepared under the same condition as the W-AS4 film was denoted as W-AS4_seed. Also, the sample with only de-ionized water (42 mL) without glycerol and $(NH_4)_2SO_4$ was denoted as the pure-H_2O sample. Finally, the obtained films were washed and dried in oven at 60 °C for 2 h.

Preparation of PB film

PB films were prepared by electrodeposition technology reported in a previous work.[70] Briefly, an electrodeposition solution contained 0.01 M $K_3[Fe(CN)_6]$, 0.01 M $FeCl_3$, and 0.05 M KCl was prepared in de-ionized water. The electrodeposition process was carried out in a three-electrode system using a CHI660E electrochemical workstation, with platinum sheet used as the counter-electrode, Ag/AgCl as the reference electrode, and the washed FTO-coated glass as the working electrode. The electrodeposition process was carried out under a current density of 50 $\mu A\ cm^{-2}$ for 300 s. After that, the FTO-coated glass with PB was washed by de-ionized water and anhydrous ethanol several times. Finally, the washed PB film was dried for 6 h under 60 °C.

Assembly of the ECD

The W-AS4 film was used as the electrochromic layer and the PB film was used as the ion storage layer. Briefly, the ECD was partly sealed with UV curing glue, with a gap of about 0.1 mm. The 1 M $LiClO_4$/PC liquid electrolyte was injected into the gap by syringe. Finally, the whole ECD was sealed with UV curing glue and black tape.

Sample characterization

The crystal structure of the WO_3 film and FTO-coated glass were examined by X-ray diffraction using a Bruker D8 ADVANCE A25X (XRD) with Cu Kα radiation. The morphologies of the samples were investigated by scanning electron microscopy (FSEM, FEI Inspect F50). The powder for the transmission electron microscopy (TEM) tests and Brunauer–Emmet–Teller (BET) surface area was synthesized by the same method as used for the film. The TEM images (low-resolution, high-resolution) were obtained using an FEI Tecnai G^2 F20 (TEM) operated at 200 KV. The BET surface area of the different structures was studied using nitrogen adsorption at 77 K (Micromeritics ASAP-2460). FT-IR spectroscopy analysis (FTIR, Thermo Fisher Scientific Nicolet iS10) was undertaken to confirm the –OH groups on the FTO surface. All the electrochemical measurements were carried out on an electrochemical workstation (CHI660E, Shanghai Chenhua Instruments, Inc.) using a conventional three-electrode test system with platinum sheet as the counter-electrode, Ag/AgCl as the reference electrode, and the WO_3 films as the working electrodes. The optical properties and kinetics from coloration and bleaching of the films were detected using a UV-vis spectrophotometer (SP60, X-Rite). 1 M $LiClO_4$ in PC was used as the electrolyte to test the electrochemical and electrochromic properties.

Conflicts of interest

There are no conflicts to declare.

Acknowledgements

We are grateful to the National Natural Science Foundation of China (Grant No. 51773027 and 21572030) and National Key R@D Program of China (No. 2017YFB0702802) for financial support.

Notes and references

1 T. S. Sian and G. B. Reddy, *Sol. Energy Mater. Sol. Cells*, 2004, **82**, 375–386.

2 P. J. Kulesza, S. Zamponi, M. A. Malik, K. Miecznikowski, M. Berrettoni and R. Marassi, *J. Solid State Electrochem.*, 1997, **1**, 88–93.

3 S. Zhang, S. Cao, T. Zhang, A. Fisher and J. Y. Lee, *Energy Environ. Sci.*, 2018, **11**, 2884–2892.

4 K. Wang, H. Wu, Y. Meng, Y. Zhang and Z. Wei, *Energy Environ. Sci.*, 2012, **5**, 8384.

5 X. Cao, C. Lau, Y. Liu, F. Wu, H. Gui, Q. Liu, Y. Ma, H. Wan, M. R. Amer and C. Zhou, *ACS Nano*, 2016, **10**, 9816–9822.

6 J. Remmele, D. E. Shen, T. Mustonen and N. Fruehauf, *ACS Appl. Mater. Interfaces*, 2015, **7**, 12001–12008.

7 D. Caruso, M. Fabretto, S. Field, D. Evans, P. Murphy, C. Hall, P. Murphy and C. Hall, *Transl. Mater. Res.*, 2015, **2**, 035002.

8 X. Chen, H. Lin, J. Deng, Y. Zhang, X. Sun, P. Chen, X. Fang, Z. Zhang, G. Guan and H. Peng, *Adv. Mater.*, 2014, **26**, 8126–8132.

9 A. M. Österholm, D. E. Shen, J. A. Kerszulis, R. H. Bulloch, M. Kuepfert, A. L. Dyer and J. R. Reynolds, *ACS Appl. Mater. Interfaces*, 2015, **7**, 1413–1421.

10 D. Ma, H. Wang, Q. Zhang and Y. Li, *J. Mater. Chem.*, 2012, **22**, 16633.

11 K. J. Patel, C. J. Panchal, M. S. Desai and P. K. Mehta, *Mater. Chem. Phys.*, 2010, **124**, 884–890.

12 D. Dini, F. Decker and E. Masetti, *J. Appl. Electrochem.*, 1996, **26**, 647–653.

13 K. Sauvet, A. Rougier and L. Sauques, *Sol. Energy Mater. Sol. Cells*, 2008, **92**, 209–215.

14 A. Rougier, K. Sauvet and L. Sauques, *Ionics*, 2008, **14**, 99–105.

15 K. Sauvet, L. Sauques and A. Rougier, *Sol. Energy Mater. Sol. Cells*, 2009, **93**, 2045–2049.

16 J. Zhang, J.-p. Tu, X.-h. Xia, X.-l. Wang and C.-d. Gu, *J. Mater. Chem.*, 2011, **21**, 5492.

17 S. Rajagopal, D. Nataraj, D. Mangalaraj, Y. Djaoued, J. Robichaud and O. Y. Khyzhun, *Nanoscale Res. Lett.*, 2009, **4**, 1335–1342.

18 D. Ma, G. Shi, H. Wang, Q. Zhang and Y. Li, *J. Mater. Chem. A*, 2013, **1**, 684–691.

19 J. Zhang, X. L. Wang, X. H. Xia, C. D. Gu and J. P. Tu, *Sol. Energy Mater. Sol. Cells*, 2011, **95**, 2107–2112.

20 Z. Jiao, X. Wang, J. Wang, L. Ke, H. V. Demir, T. W. Koh and X. W. Sun, *Chem. Commun.*, 2012, **48**, 365–367.

21 H. Kalhori, M. Ranjbar, H. Salamati and J. M. D. Coey, *Sens. Actuators, B*, 2016, **225**, 535–543.

22 S. Zhang, S. Wu, J. Wang, J. Jin and T. Peng, *Cryst. Growth Des.*, 2018, **18**, 794–801.

23 G. F. Cai, J. P. Tu, D. Zhou, X. L. Wang and C. D. Gu, *Sol. Energy Mater. Sol. Cells*, 2014, **124**, 103–110.

24 D. Nagy, D. Nagy, I. M. Szilágyi and X. Fan, *RSC Adv.*, 2016, **6**, 33743–33754.

25 F. Zheng, S. Song, F. Lu, R. Li, N. Bu, J. Liu, Y. Li, P. Hu and Q. Zhen, *CrystEngComm*, 2016, **18**, 3891–3904.

26 W. Man, H. Lu, L. Ju, F. Zheng, M. Zhang and M. Guo, *RSC Adv.*, 2015, **5**, 106182–106190.

27 H. Li, G. Shi, H. Wang, Q. Zhang and Y. Li, *J. Mater. Chem. A*, 2014, **2**, 11305–11310.

28 Z. Bi, X. Li, X. He, Y. Chen, X. Xu and X. Gao, *Sol. Energy Mater. Sol. Cells*, 2018, **183**, 59–65.

29 Y. Li, D. Chen and R. A. Caruso, *J. Mater. Chem. C*, 2016, **4**, 10500–10508.

30 A. V. Kadam, *J. Appl. Electrochem.*, 2016, **47**, 335–342.

31 Q. Ji, Y. Jiang, Z. Zhang, Y. Tian and Z. Wang, *Z. Anorg. Allg. Chem.*, 2014, **640**, 1965–1970.

32 K. O. Iwu, A. Galeckas, P. Rauwel, A. Y. Kuznetsov and T. Norby, *J. Solid State Chem.*, 2012, **185**, 245–252.

33 R. Yu, Z.-h. Meng, M.-d. Ye, Y.-h. Lin, N.-b. Lin, X.-y. Liu, W.-d. Yu and X.-y. Liu, *CrystEngComm*, 2015, **17**, 6583–6590.

34 L. Chen, S. Lam, Q. Zeng, R. Amal and A. Yu, *J. Phys. Chem. C*, 2012, **116**, 11722–11727.

35 B. Miao, W. Zeng, S. Hussain, Q. Mei, S. Xu, H. Zhang, Y. Li and T. Li, *Mater. Lett.*, 2015, **147**, 12–15.
36 L. Zhou, J. Zou, M. Yu, P. Lu, J. Wei, Y. Qian, Y. Wang and C. Yu, *Cryst. Growth Des.*, 2008, **8**, 3993–3998.
37 H. Zheng, J. Z. Ou, M. S. Strano, R. B. Kaner, A. Mitchell and K. Kalantar-zadeh, *Adv. Funct. Mater.*, 2011, **21**, 2175–2196.
38 J.-H. Ha, P. Muralidharan and D. K. Kim, *J. Alloys Compd.*, 2009, **475**, 446–451.
39 I. M. Szilágyi, J. Pfeifer, C. Balázsi, A. L. Tóth, K. Varga-Josepovits, J. Madarász and G. Pokol, *J. Therm. Anal. Calorim.*, 2008, **94**, 499–505.
40 I. M. Szilágyi, I. Sajó, P. Király, G. Tárkányi, A. L. Tóth, A. Szabó, K. Varga-Josepovits, J. Madarász and G. Pokol, *J. Therm. Anal. Calorim.*, 2009, **98**, 707–716.
41 I. M. Szilágyi, B. Fórizs, O. Rosseler, Á. Szegedi, P. Németh, P. Király, G. Tárkányi, B. Vajna, K. Varga-Josepovits, K. László, A. L. Tóth, P. Baranyai and M. Leskelä, *J. Catal.*, 2012, **294**, 119–127.
42 I. M. Szilagyi, J. Madarasz, G. Pokol, P. Kiraly, G. Tarkanyi, S. Saukko, J. Mizsei, A. L. Toth, A. Szabo and K. Varga-Josepovitso, *Chem. Mater.*, 2008, **20**, 4116–4125.
43 S. Balaji, Y. Djaoued, A. S. B. Albert, R. Z. Ferguson and R. Brüning, *Chem. Mater.*, 2009, **21**, 1381–1389.
44 W. Han, M. Hibino and T. Kudo, *Solid State Ionics*, 2000, **128**, 25–32.
45 M. Hibino, W. Han and T. Kudo, *Solid State Ionics*, 2000, **135**, 61–69.
46 K.-S. Lee, D.-K. Seo and M.-H. Whangbo, *J. Am. Chem. Soc.*, 1997, **119**, 4043–4049.
47 S. Adhikari and D. Sarkar, *J. Electrochem. Soc.*, 2014, **162**, H58–H64.
48 H. Zhang, H. Zhao, Y.-Q. Jiang, S.-Y. Hou, Z.-H. Zhou and H.-L. Wan, *Inorg. Chim. Acta*, 2003, **351**, 311–318.
49 R.-F. Mo, G.-Q. Jin and X.-Y. Guo, *Chin. J. Inorg. Chem.*, 2007, **23**, 1615–1620.
50 H. Zhang, T. Liu, L. Huang, W. Guo, D. Liu and W. Zeng, *Phys. E Low-dimens. Syst. Nanostruct.*, 2012, **44**, 1467–1472.
51 G. F. Cai, D. Zhou, Q. Q. Xiong, J. H. Zhang, X. L. Wang, C. D. Gu and J. P. Tu, *Sol. Energy Mater. Sol. Cells*, 2013, **117**, 231–238.
52 D. Nagy, T. Firkala, E. Drotár, Á. Szegedi, K. László and I. M. Szilágyi, *RSC Adv.*, 2016, **6**, 95369–95377.
53 D.-J. Kim and S.-I. Pyun, *Solid State Ionics*, 1997, **99**, 185–192.
54 W. Cheng, E. Baudrin, B. Dunn and J. I. Zink, *J. Mater. Chem.*, 2001, **11**, 92–97.
55 C. Y. Ng, K. Abdul Razak and Z. Lockman, *J. Alloys Compd.*, 2014, **588**, 585–591.
56 S. Vankova, S. Zanarini, J. Amici, F. Camara, R. Arletti, S. Bodoardo and N. Penazzi, *Nanoscale*, 2015, **7**, 7174–7177.
57 J. Zhou, Y. Wei, G. Luo, J. Zheng and C. Xu, *J. Mater. Chem. C*, 2016, **4**, 1613–1622.
58 P. Zhao, X. Ye, Y. Zhu, H. Jiang, L. Wang, Z. Yue, Z. Wan and C. Jia, *Electrochim. Acta*, 2018, **281**, 717–724.
59 S. Sallard, T. Brezesinski and B. M. Smarsly, *J. Phys. Chem. C*, 2007, **111**, 7200–7206.
60 M. Deepa, A. K. Srivastava, T. K. Saxena and S. A. Agnihotry, *Appl. Surf. Sci.*, 2005, **252**, 1568–1580.
61 S. Cong, F. Geng and Z. Zhao, *Adv. Mater.*, 2016, **28**, 10518–10528.
62 L. Shen, G. Luo, J. Zheng and C. Xu, *Electrochim. Acta*, 2018, **278**, 263–270.
63 R. Zheng, Y. Fan, Y. Wang, Z. Wan, C. Jia, X. Weng, J. Xie and L. Deng, *Electrochim. Acta*, 2018, **286**, 296–303.
64 J. Jia, X. Liu, R. Mi, N. Liu, Z. Xiong, L. Yuan, C. Wang, G. Sheng, L. Cao, X. Zhou and X. Liu, *J. Mater. Chem. A*, 2018, **6**, 15330–15339.
65 M. Yu, Y. Zeng, Y. Han, X. Cheng, W. Zhao, C. Liang, Y. Tong, H. Tang and X. Lu, *Adv. Funct. Mater.*, 2015, **25**, 3534–3540.
66 C. P. Ping Wong, C. W. Lai, K. M. Lee, J. C. Juan and S. B. Abd Hamid, *Ceram. Int.*, 2016, **42**, 13128–13135.
67 J. Yan, Q. Wang, T. Wei, L. Jiang, M. Zhang, X. Jing and Z. Fan, *ACS Nano*, 2014, **8**, 4720–4729.
68 J. H. Lee, N. Park, B. G. Kim, D. S. Jung, K. Im, J. Hur and J. W. Choi, *ACS Nano*, 2013, **7**, 9366–9374.
69 Z. Jiao, X. W. Sun, J. Wang, L. Ke and H. V. Demir, *J. Phys. D: Appl. Phys.*, 2010, **43**, 285501.
70 Z. Bi, X. Li, Y. Chen, X. He, X. Xu and X. Gao, *ACS Appl. Mater. Interfaces*, 2017, **9**, 29872–29880.